

Universal Scaling Laws for a Generic Swimmer Model. – Supplementary Material–

Bruno Ventéjou,^{1,*} Thibaut Métivet,^{2,†} Aurélie Dupont,¹ and Philippe Peyla^{1,‡}

¹*Univ. Grenoble Alpes, CNRS, LIPhy, 38000 Grenoble, France*

²*Univ. Grenoble Alpes, Inria, CNRS, Grenoble INP, LJK, 38000 Grenoble, France*

(Dated: September 19, 2024)

I. 2D SCALING

A. Scaling laws

Our scaling arguments are still valid in 2D, as they are based on force and torque densities. Note that in 2D, the mass density ρ has dimensions $[mass][length]^{-2}$, the force density f_0 has $[Newton][length]^{-2} = [mass][length]^{-1}[time]^{-2}$ and the viscosity η has $[Newton][length]^{-1}[time] = [mass][time]^{-1}$. Therefore, the thrust number $Th = \rho f_0 L^3 / \eta^2$ is still dimensionless.

In the Stokes regime ($Re < 1$), the Stokes force is still balanced by the viscous drag, which however contains logarithmic terms coming from 2D integration. The force density thus scales as $f_0 L^2 \sim \eta v / \log(Re) = \eta^2 Re / (\rho L \log(Re))$ (using $v = \eta Re / (\rho L)$). Since the log function does not contribute to the scaling, we still have $Re \sim Th$.

In the laminar regime, we have $f_0 L^2 \sim (\eta v / \delta) L$, which still leads to $Re \sim Th^{2/3}$. Finally, in the turbulent regime, we have $f_0 L^2 \sim \rho v^2 L$ which again lead to the same scaling $Re \sim Th^{1/2}$.

B. Numerical simulations

Figure ?? shows the Reynolds number Re as a function of the thrust number Th in 2D. The three regimes obtained numerically match the hydrodynamic scaling laws described above. The transition from the Stokes regime to the laminar regime slightly deviates from a power law, which may be related to the logarithmic correction in $f_0 L^2 \sim \eta v / \log(Re)$.

* bruno.ventejou@univ-grenoble-alpes.fr

† thibaut.metivet@inria.fr

‡ philippe.peyla@univ-grenoble-alpes.fr

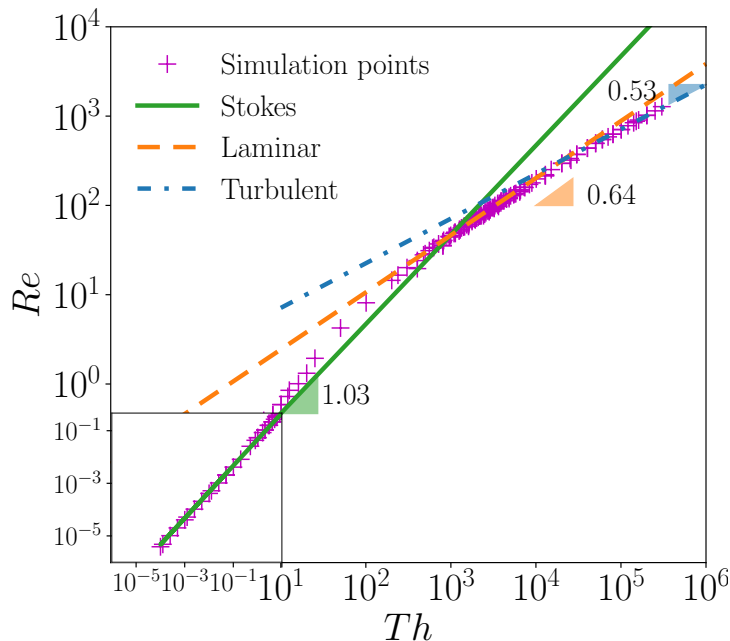


FIG. 1. Re as a function of Th for 2D numerical simulations (crosses). We clearly obtain three regimes: $Re \sim Th^{1.03}$ for $Re \lesssim 0.5$; $Re \sim Th^{0.64}$ for $40 \lesssim Re \lesssim 400$ and $Re \sim Th^{0.53}$ for $Re \gtrsim 400$. The three lines correspond to fitted curves and give the numerical scaling exponents. Note that the crossovers of the different regimes depend on the geometry of the swimmer: the aspect ratio for these simulations is $a_r = 2$.

II. NUMERICAL MODEL

A. Fluid-solid coupling

Let us consider a domain $\Omega \in^d$ ($d = 2, 3$) filled with an incompressible fluid of density ρ_f and viscosity η_f , containing a swimming rigid body $\mathcal{B} \subset \Omega$ with density ρ_b and center-of-mass \mathbf{X}_B . The swimming body acts on the surrounding fluid with a swimming force $\mathbf{F}_t = \mathbf{F}(t)\delta_{\mathbf{X}_t}$ and torque $\mathbf{T}_t = \mathbf{T}(t)\delta_{\mathbf{X}_t}$ (with $\delta_{\mathbf{X}}(\mathbf{x}) \equiv \delta(\mathbf{x} - \mathbf{X})$ the dirac distribution centered at \mathbf{X}), applied at \mathbf{X}_t (representing the position of the tail of the swimmer). Assuming a Newtonian constitutive law, the fluid phase therefore obeys the incompressible Navier-Stokes equations, with no-slip boundary conditions on the interface with the rigid body:

$$\rho_f \frac{D\mathbf{v}}{Dt} - \nabla \cdot (2\eta_f \mathbf{E}(\mathbf{v})) + \nabla p = \mathbf{f}_f + \mathbf{F}_t + \mathbf{T}_t \quad \text{in } \Omega \setminus \mathcal{B}, \quad (1)$$

$$\nabla \cdot \mathbf{v} = 0 \quad \text{in } \Omega \setminus \mathcal{B}, \quad (2)$$

$$\mathbf{v}(\mathbf{x}) = \mathbf{V}_B + \boldsymbol{\omega}_B \times (\mathbf{x} - \mathbf{X}_B) \quad \text{on } \partial\mathcal{B}, \quad (3)$$

where D/Dt is the material derivative

$$D\mathbf{v}/Dt \equiv \partial\mathbf{v}/\partial t + (\mathbf{v} \cdot \nabla)\mathbf{v},$$

$\mathbf{E}(\mathbf{v})$ is the strain-rate tensor

$$\mathbf{E}(\mathbf{v}) \equiv \frac{\nabla\mathbf{v} + \nabla\mathbf{v}^t}{2},$$

\mathbf{f}_f are external volumic forces (e.g. gravity $\mathbf{f}_f = \rho_f \mathbf{g}$), \mathbf{X}_B is the center of mass of the body, and \mathbf{V}_B and $\boldsymbol{\omega}_B$ are its translation and angular velocities, respectively.

The equations of motion for the rigid body are then the Newton-Euler equations

$$M_{\mathcal{B}} \frac{d\mathbf{V}_{\mathcal{B}}}{dt} = \mathbf{f}_b + \mathbf{F}_f - \mathbf{F}_{\mathcal{B}} \quad (4)$$

$$\frac{d(\mathbf{I}_{\mathcal{B}}\boldsymbol{\omega}_{\mathcal{B}})}{dt} \equiv \mathbf{I}_{\mathcal{B}} \frac{d\boldsymbol{\omega}_{\mathcal{B}}}{dt} + \boldsymbol{\omega}_{\mathcal{B}} \times \mathbf{I}_{\mathcal{B}}\boldsymbol{\omega}_{\mathcal{B}} = \mathbf{m}_f - \mathbf{T}_{\mathcal{B}} \quad (5)$$

where $M_{\mathcal{B}}$ and $\mathbf{I}_{\mathcal{B}}$ are respectively the mass and (spatial) inertia tensor of \mathcal{B} :

$$M_{\mathcal{B}} = \int_{\mathcal{B}} \rho_b \quad (6)$$

$$\mathbf{I}_{\mathcal{B}} = \int_{\mathcal{B}} \rho_b (\|\mathbf{x} - \mathbf{X}_{\mathcal{B}}\|^2 - (\mathbf{x} - \mathbf{X}_{\mathcal{B}}) \otimes (\mathbf{x} - \mathbf{X}_{\mathcal{B}})) \quad (7)$$

The right-hand sides correspond to the forces $\mathbf{F}_f - \mathbf{F}_{\mathcal{B}}$ and moments $\mathbf{m}_f - \mathbf{T}_{\mathcal{B}}$ exerted by the fluid on the swimmer, with

$$\begin{aligned} \mathbf{F}_f &= - \int_{\partial\mathcal{B}} \boldsymbol{\sigma} \mathbf{n} ds \\ \mathbf{m}_f &= - \int_{\partial\mathcal{B}} (\mathbf{x} - \mathbf{X}_{\mathcal{B}}) \times \boldsymbol{\sigma} \mathbf{n} ds \end{aligned}$$

and the active force $-\mathbf{F}_{\mathcal{B}} = -\mathbf{F}(t)\delta_{\mathbf{X}_{\mathcal{B}}}$ and torque $-\mathbf{T}_{\mathcal{B}} = -\mathbf{T}(t)\delta_{\mathbf{X}_{\mathcal{B}}}$ applied at the center-of-mass of the swimmer, and opposing the swimming force and torque, are the consequence of the third Newton's law, the whole "fluid+body" system being isolated.

Note that the constraint of rigidity of the body imposes that the velocity field inside \mathcal{B} also obeys ??, i.e. $\mathbf{v}(\mathbf{x}) = \mathbf{V}_{\mathcal{B}} + \boldsymbol{\omega}_{\mathcal{B}} \times (\mathbf{x} - \mathbf{X}_{\mathcal{B}})$ in \mathcal{B} , or equivalently

$$\mathbf{E}(\mathbf{v}) = 0 \quad \text{in } \mathcal{B}. \quad (8)$$

A *fictitious domain* variational formulation of the fluid-rigid body coupling can thus be written on the whole domain Ω as (c.f. [? ?])

$$\begin{aligned} \int_{\Omega} \rho \frac{D\mathbf{v}}{Dt} \cdot \tilde{\mathbf{v}} + \int_{\Omega} 2\eta_f \mathbf{E}(\mathbf{v}) : \mathbf{E}(\tilde{\mathbf{v}}) - \int_{\Omega} p \boldsymbol{\nabla} \cdot \mathbf{v} &= \int_{\Omega} (\mathbf{f} + \mathcal{F} + \mathcal{T}) \cdot \tilde{\mathbf{v}} & \forall \tilde{\mathbf{v}} \in \mathcal{V}_{\mathcal{B}}(\Omega) \\ \int_{\Omega} q \boldsymbol{\nabla} \cdot \mathbf{v} &= 0 & \forall q \in L^2(\Omega) \end{aligned} \quad (9)$$

where ρ and \mathbf{f} are the extended density and volumic force fields

$$\rho = \rho_f \chi_{\Omega \setminus \mathcal{B}} + \rho_b \chi_{\mathcal{B}} \quad (10)$$

$$\mathbf{f} = \mathbf{f}_f \chi_{\Omega \setminus \mathcal{B}} + \mathbf{f}_b \chi_{\mathcal{B}} \quad (11)$$

with χ_S the indicator function of the set S , \mathcal{F} and \mathcal{T} denote the active force and torque dipoles

$$\mathcal{F} \equiv \mathbf{F}_t - \mathbf{F}_{\mathcal{B}} = \mathbf{F}(t) (\delta_{\mathbf{X}_t} - \delta_{\mathbf{X}_{\mathcal{B}}}) \quad (12)$$

$$\mathcal{T} \equiv \mathbf{T}_t - \mathbf{T}_{\mathcal{B}} = \mathbf{T}(t) (\delta_{\mathbf{X}_t} - \delta_{\mathbf{X}_{\mathcal{B}}}) \quad (13)$$

and $\mathcal{V}_{\mathcal{B}}(\Omega)$ is the space of velocities on Ω which satisfy the rigid body constraints inside \mathcal{B}

$$\mathcal{V}_{\mathcal{B}}(\Omega) = \{\mathbf{v} \in H^1(\Omega)^d; \mathbf{E}(\mathbf{v}) = 0 \text{ in } \mathcal{B}\}.$$

To enforce the rigid-body constraint required in the test space $\mathcal{V}_{\mathcal{B}}(\Omega)$, we use a penalty method inspired from [?], which can in practice be implemented simply by introducing a spatially-dependent viscosity field :

$$\eta(\mathbf{x}) = \eta_f \chi_{\Omega \setminus \mathcal{B}} + \eta_b \chi_{\mathcal{B}} \quad (14)$$

where η_b denote some large viscosity value, chosen in practice as $\eta_b = [10^3 - 10^6]\eta_f$ in our simulations. The corresponding variational formulation is then simply obtained by replacing the fluid viscosity η_f with η in ??, leading to the unconstrained formulation

$$\begin{aligned} \int_{\Omega} \rho \frac{D\mathbf{v}}{Dt} \cdot \tilde{\mathbf{v}} + \int_{\Omega} 2\eta \mathbf{E}(\mathbf{v}) : \mathbf{E}(\tilde{\mathbf{v}}) - \int_{\Omega} p \nabla \cdot \mathbf{v} &= \int_{\Omega} (\mathbf{f} + \mathcal{F} + \mathcal{T}) \cdot \tilde{\mathbf{v}} & \forall \tilde{\mathbf{v}} \in H_0^1(\Omega)^d, \\ \int_{\Omega} q \nabla \cdot \mathbf{v} &= 0 & \forall q \in L^2(\Omega). \end{aligned} \quad (15)$$

In order to solve ?? with standard finite-element methods while preserving optimal convergence orders [?], we regularize the characteristic and delta functions by using the level-set framework of [?], which gives

$$\chi_{\mathcal{B}}^{\varepsilon}(\mathbf{x}) = \begin{cases} 1 & \text{if } \phi_{\mathcal{B}}(\mathbf{x}) \leq -\varepsilon \\ \frac{1}{2} \left(1 - \frac{\phi_{\mathcal{B}}(\mathbf{x})}{\varepsilon} - \frac{\sin\left(\frac{\pi\phi_{\mathcal{B}}(\mathbf{x})}{\varepsilon}\right)}{\pi} \right) & \text{if } -\varepsilon \leq \phi_{\mathcal{B}}(\mathbf{x}) \leq \varepsilon \\ 0 & \text{if } \varepsilon \leq \phi_{\mathcal{B}}(\mathbf{x}) \end{cases} \quad (16)$$

$$\delta_{\mathbf{X}}^{\varepsilon}(\mathbf{x}) = \begin{cases} \alpha_d(\varepsilon) \left(1 + \cos\left(\frac{\pi\|\mathbf{x} - \mathbf{X}\|}{\varepsilon}\right) \right) & \text{if } \|\mathbf{x} - \mathbf{X}\| \leq \varepsilon \\ 0 & \text{if } \varepsilon \leq \|\mathbf{x} - \mathbf{X}\| \end{cases} \quad (17)$$

where $\phi_{\mathcal{B}}$ denotes the signed distance function to the boundary $\partial\mathcal{B}$ of the body, and $\alpha_d(\varepsilon)$ is a normalization constant which depends on the dimension d of space:

$$\alpha_2(\varepsilon) = \frac{\pi}{\pi^2 - 4} \frac{1}{\varepsilon^2} \quad \text{and} \quad \alpha_3(\varepsilon) = \frac{3}{4} \frac{\pi}{\pi^2 - 6} \frac{1}{\varepsilon^3}.$$

Note that for non-spherical bodies, the signed distance function $\phi_{\mathcal{B}}$ is in general not analytic, but can be efficiently computed numerically with a fast-marching algorithm [?]. We use in practice the parallel unstructured algorithm described in [?] and implemented in the FEEL++ library [?].

The corresponding regularized density, viscosity are then defined accordingly as

$$\rho^{\varepsilon} = \rho_f + (\rho_b - \rho_f) \chi_{\mathcal{B}}^{\varepsilon} \quad (18)$$

$$\eta^{\varepsilon} = \eta_f + (\eta_b - \eta_f) \chi_{\mathcal{B}}^{\varepsilon}. \quad (19)$$

The force dipole term is also straightforwardly regularized as

$$\mathcal{F}^{\varepsilon} \equiv \mathbf{F}(t) (\delta_{\mathbf{X}_t}^{\varepsilon} - \delta_{\mathbf{X}_B}^{\varepsilon}), \quad (20)$$

while the torque dipole is rewritten with regularized rotlets, taking inspiration from the singularity expansion method for Stokes flows [?]. Defining

$$\mathbf{T}_{\mathbf{X}}^{\varepsilon} \equiv \frac{1}{2} \nabla \times (\mathbf{T} \delta_{\mathbf{X}}^{\varepsilon}), \quad (21)$$

one can easily check that the imposed torque indeed corresponds to \mathbf{T} , leading to the natural regularization of the torque dipole as

$$\mathcal{T}^{\varepsilon} \equiv \frac{1}{2} \nabla \times (\mathbf{T} (\delta_{\mathbf{X}_t}^{\varepsilon} - \delta_{\mathbf{X}_B}^{\varepsilon})). \quad (22)$$

Note that the corresponding integral in the variational formulation ?? can be integrated by parts to avoid differentiating δ^{ε} , and rewritten as

$$\int_{\Omega} \mathcal{T} \cdot \tilde{\mathbf{v}} = \frac{1}{2} \int_{\Omega} \mathbf{T} (\delta_{\mathbf{X}_t}^{\varepsilon} - \delta_{\mathbf{X}_B}^{\varepsilon}) \cdot (\nabla \times \tilde{\mathbf{v}}).$$

We can then discretize the weak incompressible Navier-Stokes equations ?? with standard inf-sup stable Taylor-Hood velocity-pressure Lagrange $\mathcal{P}_2^d - \mathcal{P}_1$ elements (see e.g. [?]), defined on an unstructured triangular (2D) or tetrahedral (3D) mesh of Ω . We use a fully implicit numerical discretization, with an order-2 backward differentiation scheme for the partial time differential term, as described in [?].

B. Swimming forces and torques

As discussed in the main text, our model relies on a pusher-like periodic force dipole, mainly responsible for propulsion and reminiscent of the fluid drainage generated by the undulatory motion of the body of a fish, along with a torque dipole mimicking the stroke of the tail, at the origin of the vortex alley in the wake of swimming fish. Both dipoles are collocated, with forces and torques applied at \mathbf{X}_t – the position of the tail – and \mathbf{X}_B – the center-of-mass of the swimmer, as stated in [?], and defined with local values

$$\mathbf{F}(t) = \frac{\pi}{2} \mathbf{F}_0 |\cos(\omega t)| \quad (23)$$

$$\mathbf{T}(t) = \mathbf{T}_0 \cos(\omega t). \quad (24)$$

C. Rigid body motion

The position and orientation of the rigid body are classically represented by its center-of-mass \mathbf{X}_B and a unit quaternion $\mathcal{B} \equiv (q_{B0}, \mathbf{q}_B) \in \mathbb{S}^3$, $\mathcal{B} \cdot \mathcal{B} = 1$, which encodes the rotation between the current and reference states (see e.g. [?]). These quantities naturally evolve in time with respectively the translation and angular velocities as

$$\frac{d\mathbf{X}_B}{dt} = \mathbf{V}_B \quad (25)$$

$$\frac{d\mathcal{B}}{dt} = \left(0, \frac{\boldsymbol{\omega}_B}{2}\right) \circ \mathcal{B} \quad (26)$$

where \circ denotes the usual quaternion product. At the discrete level, these equations can be integrated on the domain \mathcal{B} given translational and rotational velocities \mathbf{V} and $\boldsymbol{\omega}$ approximating \mathbf{V}_B and $\boldsymbol{\omega}_B$; we use in practice a first-order Euler scheme for the translation part, and a first order Lie-Euler scheme for the rotation part, which gives the update:

$$\begin{aligned} \mathbf{X}_B^{n+1} &= \mathbf{X}_B^n + \delta t \mathbf{V}_B^{n+1} \\ \mathcal{B}^{n+1} &= \left(0, \frac{\boldsymbol{\omega}_B^{n+1} \delta t}{2}\right) \circ \mathcal{B}^n. \end{aligned} \quad (27)$$

The translation and angular velocities of the immersed rigid body can be straightforwardly computed from the “virtual” fluid velocity inside the body domain: recalling that $\mathbf{v}(\mathbf{x}) = \mathbf{V}_B + \boldsymbol{\omega}_B \times (\mathbf{x} - \mathbf{X}_B)$ in \mathcal{B} , we have

$$\mathbf{V}_B = \frac{1}{M_B} \int_{\mathcal{B}} \rho_b \mathbf{v} \quad (28)$$

$$\boldsymbol{\omega}_B = \mathbf{I}_B^{-1} \int_{\mathcal{B}} \rho_b (\mathbf{x} - \mathbf{X}_B) \times \mathbf{v}. \quad (29)$$

Note that to ensure decoupling between the translation and rotation motion in the discrete regularized setting, these equations need to be consistently evaluated with the corresponding regularized quantities, as detailed in [?] below.

D. Coupling algorithm

We couple the fluid and rigid-body dynamics with a semi-implicit scheme, summarized in [?]. The resulting system is implemented and solved using the highly parallel finite-element library FEEL++ [?].

Algorithm 1: Fluid-solid coupling

parameters : $\rho_f, \rho_b, \eta_f, \eta_b; \delta t, \varepsilon$
input : $t^n; \mathcal{B}^n \sim (\mathbf{X}_{\mathcal{B}^n, \mathcal{B}^n}); (\mathbf{v}^n, p^n), (\mathbf{V}_{\mathcal{B}^n}^n, \boldsymbol{\omega}_{\mathcal{B}^n}^n)$
output : $t^{n+1}; \mathcal{B}^{n+1} \sim (\mathbf{X}_{\mathcal{B}^{n+1}, \mathcal{B}^{n+1}}); (\mathbf{v}^{n+1}, p^{n+1}), (\mathbf{V}_{\mathcal{B}^{n+1}}^{n+1}, \boldsymbol{\omega}_{\mathcal{B}^{n+1}}^{n+1})$
 $\phi \leftarrow \text{SignedDistance}(\mathcal{B}^n);$
 $\chi_{\mathcal{B}}^\varepsilon \leftarrow \chi_{\mathcal{B}}^\varepsilon[\phi];$??
 $\rho^\varepsilon \leftarrow \rho_f + (\rho_b - \rho_f)\chi_{\mathcal{B}}^\varepsilon;$??
 $\eta^\varepsilon \leftarrow \eta_f + (\eta_b - \eta_f)\chi_{\mathcal{B}}^\varepsilon;$??
 $\mathcal{F}^\varepsilon \leftarrow \mathbf{F}(t^n) (\delta_{\mathbf{X}_t}^\varepsilon - \delta_{\mathbf{X}_{\mathcal{B}}}^\varepsilon);$????
 $\mathcal{T}^\varepsilon \leftarrow \mathbf{T}(t^n) (\delta_{\mathbf{X}_t}^\varepsilon - \delta_{\mathbf{X}_{\mathcal{B}}}^\varepsilon);$????
 $(\mathbf{v}^{n+1}, p^{n+1}) \leftarrow \text{SolveNavierStokes}(\mathbf{v}^n, p^n, \mathcal{F}^\varepsilon, \mathcal{T}^\varepsilon; \rho^\varepsilon, \eta^\varepsilon);$??
 $M_{\mathcal{B}}^\varepsilon \leftarrow \int_{\Omega} \rho^\varepsilon \chi_{\mathcal{B}}^\varepsilon;$
 $\mathbf{X}_{\mathcal{B}}^\varepsilon \leftarrow \frac{1}{M_{\mathcal{B}}^\varepsilon} \int_{\Omega} \rho^\varepsilon \mathbf{x} \chi_{\mathcal{B}}^\varepsilon;$
 $\mathbf{I}_{\mathcal{B}}^\varepsilon \leftarrow \int_{\Omega} \rho^\varepsilon (\|\mathbf{x} - \mathbf{X}_{\mathcal{B}}^\varepsilon\|^2 - (\mathbf{x} - \mathbf{X}_{\mathcal{B}}^\varepsilon) \otimes (\mathbf{x} - \mathbf{X}_{\mathcal{B}}^\varepsilon)) \chi_{\mathcal{B}}^\varepsilon;$
 $\mathbf{V}_{\mathcal{B}}^{n+1} \leftarrow \frac{1}{M_{\mathcal{B}}^\varepsilon} \int_{\Omega} \rho^\varepsilon \mathbf{v}^{n+1} \chi_{\mathcal{B}}^\varepsilon;$??
 $\boldsymbol{\omega}_{\mathcal{B}}^{n+1} \leftarrow \mathbf{I}_{\mathcal{B}}^{\varepsilon^{-1}} \int_{\Omega} \rho^\varepsilon (\mathbf{x} - \mathbf{X}_{\mathcal{B}}^\varepsilon) \times \mathbf{v}^{n+1} \chi_{\mathcal{B}}^\varepsilon;$??
 $(\mathbf{X}_{\mathcal{B}^{n+1}, \mathcal{B}^{n+1}}) \leftarrow \text{MoveRigidBody}(\mathbf{V}_{\mathcal{B}^{n+1}}^{n+1}, \boldsymbol{\omega}_{\mathcal{B}^{n+1}}^{n+1});$??
 $t^{n+1} = t^n + \delta t;$

E. Simulations details and parameters

We use in practice a rigid body with an ellipsoidal shape to perform simulations of our swimmer model. The shape of the swimmer is parametrized by the aspect ratio a_r , which is the ratio between the semi-major axis $L/2$ and the semi-minor axis b . In practice, we use $a_r \in \llbracket 2, 8 \rrbracket$. While the aspect ratio does not impact the scaling laws presented in the results, it plays an important role in the crossover transitions between the different regimes, and in the value of the prefactors in the scaling laws. It also plays a key role for the stability of the trajectory at high Re , due to the coupling of the von Karman vortex street with the wake of the swimmer.

The ellipsoidal shape is initially defined in Cartesian space by the implicit surface

$$\frac{4x^2}{L^2} + \frac{y^2}{b^2} + \frac{z^2}{b^2} = 1.$$

Initially, the orientation $\mathbf{p}_{\mathcal{B}}$ is given by the unit vector $\mathbf{x}_0 = (1, 0, 0)$, and we define the quaternion $\mathbf{x}_0 = (0, \mathbf{x}_0)$. The ellipsoid is then evolved in time following the coupling algorithm ??.

In all simulations, the distance between the tail \mathbf{X}_t and the center of mass $\mathbf{X}_{\mathcal{B}}$ is fixed according to the aspect ratio a_r as follow

$$\|\mathbf{X}_t - \mathbf{X}_{\mathcal{B}}\| = \frac{L}{2} (1 + 2a_r^{-1}).$$

It is also possible to control the direction of the swimmer by turning the position of the tail with respect to the orientation of the body: given some unit quaternion ${}_t$ encoding the orientation of the tail, the position of the tail \mathbf{X}_t can be computed as

$$(0, \mathbf{X}_t) = (0, \mathbf{X}_{\mathcal{B}}) + {}_t \left(-\frac{L}{2} (1 + 2a_r^{-1}) (0, \mathbf{p}_{\mathcal{B}}^n) \right) {}_t^{-1}.$$

where $\mathbf{p}_{\mathcal{B}}^n$ is the current orientation of the swimmer. If the swimmer is going straight the equation reduces to $\mathbf{X}_t = \mathbf{X}_{\mathcal{B}} - \frac{L}{2} (1 + 2a_r^{-1}) \mathbf{p}_{\mathcal{B}}^n$.

While the force and torque dipoles appear independent in the model, we ensure realistic values by scaling them according to the characteristic size of the swimmer. In practice, we enforce

$$\|\mathbf{T}_0\| = \beta L \|\mathbf{F}_0\|$$

where the constant βL reflects the size of tail and the efficiency to produce thrust. This value is expected to depend strongly on the species, and we have arbitrarily chosen $\beta L = 1$ (i.e. $\|\mathbf{T}_0\| = \|\mathbf{F}_0\|$) in our simulations, as we found that this value reproduces realistic reverse von Karman vortex wakes, and leads to stable trajectories. If $\|\mathbf{F}_0\|/\|\mathbf{T}_0\|$ is too small, the vortex do not evacuate fast enough and start to form pairs going in random direction. The swimmer then moves erratically in space. This behavior is not physical and is a consequence of the model, which is much more general than actual aquatic organisms, for which the space parameter is largely reduced by the biological and kinematic constrains.

III. MANEUVERABILITY

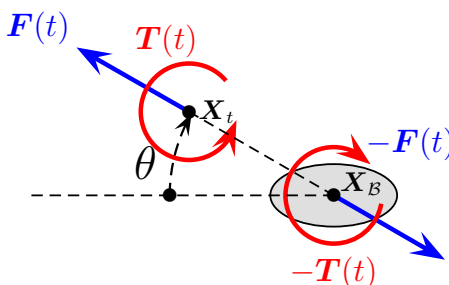


FIG. 2. Controlling the trajectory of the swimmer: the orientation of the “phantom tail” can be adjusted with respect to the orientation of the body with some angle θ , enabling turning motion.

If the force dipole makes an angle θ with the direction of the swimmer (major axis of the ellipsoid) (see Fig. ??), the swimmer can turn and describe circular trajectories (see Fig. ??). The radius of curvature of this trajectory depends on f_0 and θ , as shown in Fig. ?. This provides maneuverability to the model, and can help the individual avoiding obstacles, walls or other swimmers. It also demonstrates the flexibility and versatility of the model, which can be used to model a swimmer in complex situations or environments.

IV. NUMERICAL STUDIES

A. Impact of the torque

The hydrodynamic scaling laws presented in the main text show the evolution of the Reynolds number Re as a function of the thrust number Th , which does not take into account the value of the torque τ_0 . Figure ?? shows the results of simulations run with different torque values, varied within more than a decade. We observe that the change in Re is only a small percentage of the change in speed due to the oscillating trajectory. Both 2D and 3D simulations display the same behavior, which shows that the torque plays no major role in controlling the velocity (or Re) of the swimmer.

B. Impact of the pulsation

Similarly, we evaluate the impact of the pulsation ω on the evolution of the Reynolds number as a function of the thrust number by comparing the swimming velocities obtained for several values of

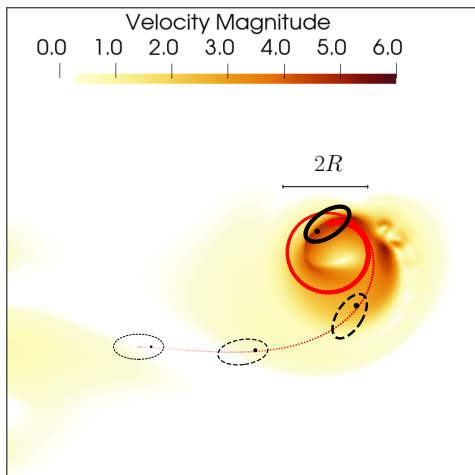


FIG. 3. Circular trajectory obtained in a 2D numerical simulation, obtained for a steering angle $\theta = 6^\circ$, and $\|\mathbf{F}_0\| = 160$. The radius of curvature R characterizes the trajectory. Dashed lines correspond to the position of the rigid body at previous times. The thicker the dotted lines, the closer it is to the current time, drawn as a solid line.

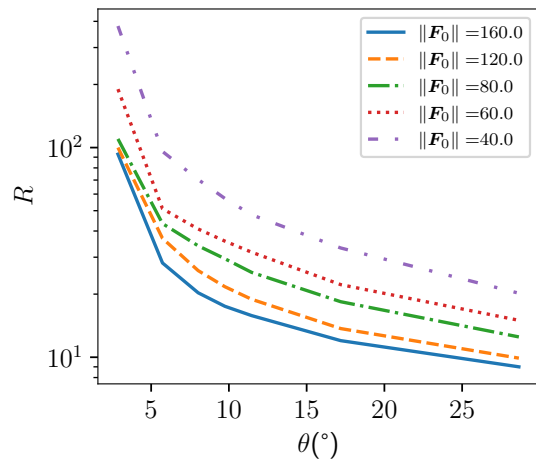


FIG. 4. Maneuverability: dependence of the radius of curvature R on the steering angle θ and the force $\|\mathbf{F}_0\|$ obtained for 2D numerical simulations.

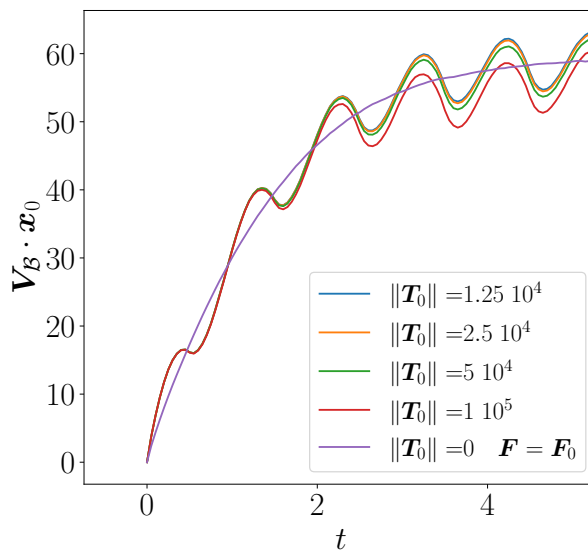


FIG. 5. Evolution of the velocity of the swimmer as a function of time in 3D simulation for different torque values. Simulations were performed with $\omega = \pi$, $\|\mathbf{F}_0\| = 6.3 \cdot 10^4$ and $L = 32$. They correspond to $Re = 1880$, which falls in the turbulent regime.

ω . The results shown in Figure ?? indicated that the pulsation does not play any role and only the time-averaged value of \mathbf{F}_0 is relevant for the $Re(Th)$ scaling.

C. Study of the aspect ratio

As discussed in Sec. ??, the aspect ratio a_r plays an important role in controlling the drag of the swimmer, in particular in the turbulent regime, where it largely affects the turbulent transition. Figure ??

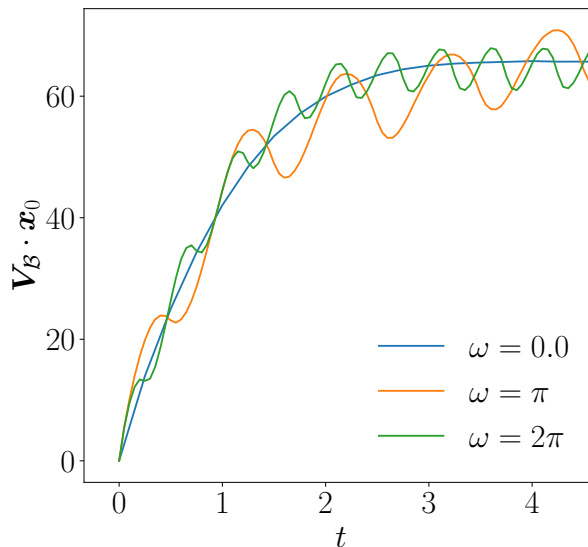


FIG. 6. Evolution of the swimming velocity as a function of time for 3D simulation and various pulsations ω . Simulation were performed with $\|\mathbf{T}_0\| = 3 \cdot 10^5$, $\|\mathbf{F}_0\| = 1.5 \cdot 10^5$ and $L = 32$, and correspond to $Re = 2080$, which falls in the turbulent regime. Note that $\omega = 0.0$ corresponds to the time-averaged dipole $\mathbf{F}(t) = \mathbf{F}_0$.

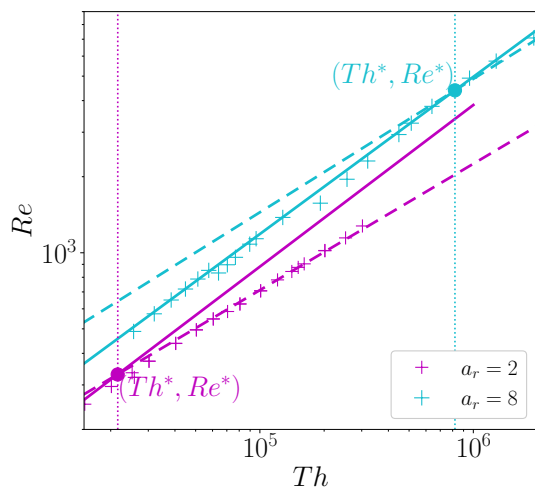


FIG. 7. Evolution of the transition between the laminar and turbulent regime for different aspect ratio values. The data correspond to 2D numerical simulations, obtained for aspect ratios $a_r = 2$ (pink) or $a_r = 8$ (blue). The solid and dashed lines are the fits of the data in the laminar regime and turbulent regimes respectively. The vertical dotted lines indicate the intersections between the plain lines and the dashed lines, which define the crossover Reynolds number Re^* .

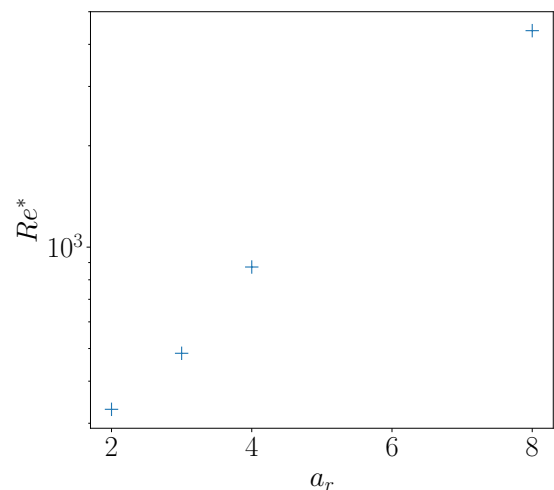


FIG. 8. Evolution of the laminar-turbulent crossover Reynolds number Re^* as a function of a_r .

shows the effect of the aspect ratio on the hydrodynamic scaling laws. While the aspect ratio does not change the exponent of the different regimes, it changes the Th value where the transition occurs. In Fig. ??, the Th value at which the transition between the laminar and the turbulent regime occurs increases with increasing aspect ratio a_r .

When a rigid body is moving in a fluid in the turbulent regime, it is possible to see a turbulent von

Karman vortex street behind the body. This effect will change a lot the evacuation of the vortex generated by the torque \mathbf{T}_0 at the rear of the body. In that case, even if the tail is in the neutral position ($\theta = 0$), the rigid body will not go straight. The effect is delayed as the aspect ratio increases. We believe this is a side effect of the model, as real swimmers moving in a turbulent regime have in general a very high aspect ratio (with a non ellipsoidal body shape) to avoid the von Karman vortex street.

V. EXPERIMENTAL DATABASE

The goal of the database is to link the swimming speed (Re) to kinematic parameters (Sw) for different aquatic organisms across a wide range of $Re \sim 10^{-9} - 10^7$. To this aim, we have collected data for which values for the velocity v , the frequency $\omega/2\pi$, the oscillation amplitude A , the size L and the viscosity η are available. At low Re , trajectory are not always rectilinear, or are subjected to noise and the velocity is reported only when it corresponds to the instantaneous velocity.

A. $Re > 1$ database construction

The main part of the database for these two regimes (laminar and turbulent) was already built in [?]] and the data are extracted from their supplementary information. Below, we summarize the origin of the data but do not give other information. The full database is available here in a *.tsv* format.

The fish database is composed of data on:

- Dace, trout and goldfish from [?]
- Mackerel from [?]
- Sturgeon from [?]
- Rainbow trout from [?]
- Giant blue fine tuna from [?]
- Saithe and mackerel from [?]
- Sharks from [?]
- Stingray from [?]
- African lungfish from [?]

The mammals database is composed of data on:

- Cetaceans from [?]
- Seals from [?]
- Manatees from [?]
- Fin whales from [? ?]
- Blue whales from [?]

The birds database is composed of data on:

- Penguins from [? ?]

The amphibians database is composed of data on:

- Tadpoles from [?]

The reptiles database is composed of data on:

- American alligator from [?]

The larvae database is composed of data on:

- Larval zebrafish from [? ? ?]
- Ascidian larvae from [? ?]
- Mayfly larvae from [?]

B. Stokes regime database construction

In this section we report all the raw data used to built the database corresponding to the Stokes regime.

The sperm cells database is composed of data on:

- Lytechinus spermatozoa from [?]
- Bull spermatozoa from [?]
- Ciona spermatozoa from [? ?]
- Lytechinus spermatozoa from [? ?]

The algae database is composed of data on:

- Chlamydomonas reinhardtii from [?]

The worms database is composed of data on:

- Caenorhabditis Elegans from [?]
- Leeches from [?]

The bacteria database is composed of data on:

- Escherichia coli from [?]